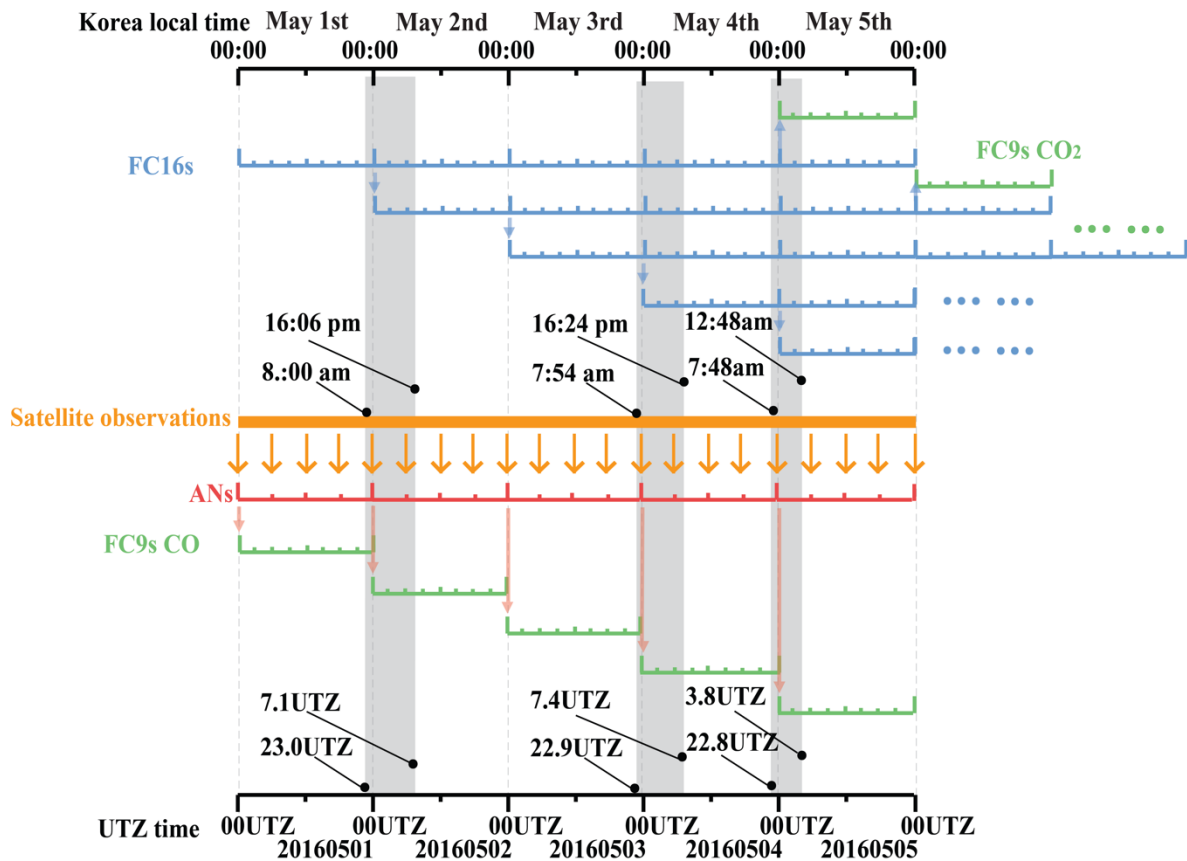Atmospheric
Chemistry
and Physics

Supplement of

Evaluating high-resolution forecasts of atmospheric CO and CO$_2$ from a global prediction system during KORUS-AQ field campaign

Wenfu Tang et al.

*Correspondence to:* Wenfu Tang (wenfutang@email.arizona.edu)

**Figure S1**. CAMS configuration. Left panel corresponds to the time configuration of the CAMS CO and CO2 evaluated in this study. The black lines represent Korea local time (on the top) and UTC time (on the bottom). The blue lines represent CAMS 5-day FC16s. FC16s are initialized with forecasts from the previous day. The orange line represents satellite observations (i.e., CO from MOPITT and IASI, CO2 from GOSAT) assimilated in CAMS (ANs). Gray shade denotes campaign time of the DC-8 aircraft. A typical DC-8 flight starts at 8am Korea time (23 UTC of previous day) and ends at 4pm Korea time (7 UTC).
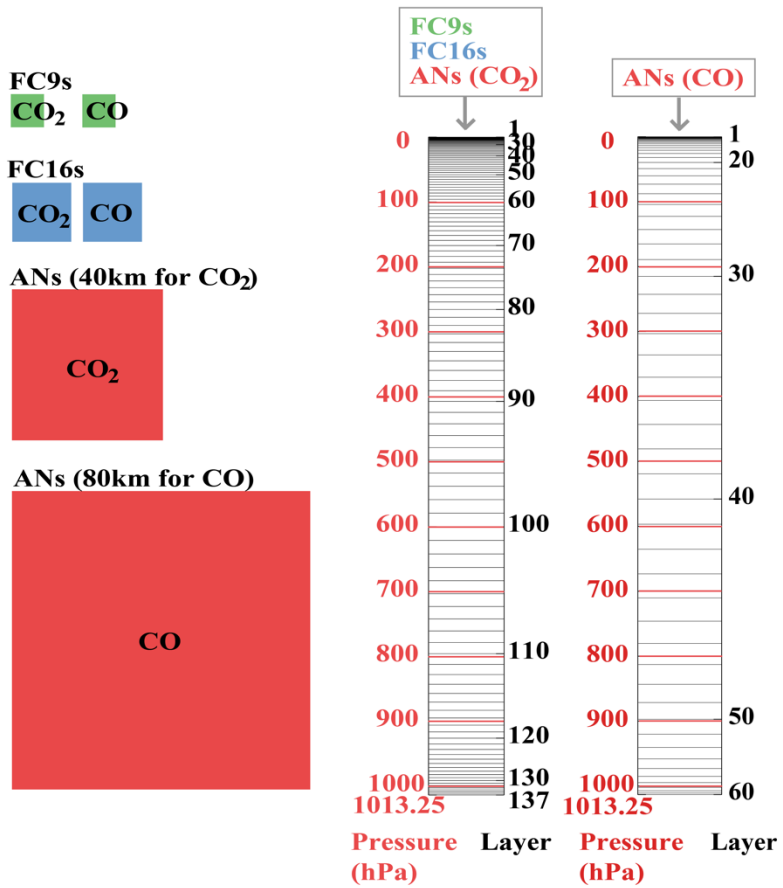
Figure S2. Model grid sizes of the CAMS and vertical structures of the model layers assuming the surface pressure being 1013.25hPa. FC9s, FC16s, and ANs for CO_2 (40 km) have 137 vertical layers. ANs for CO (80 km) have 60 vertical layers.
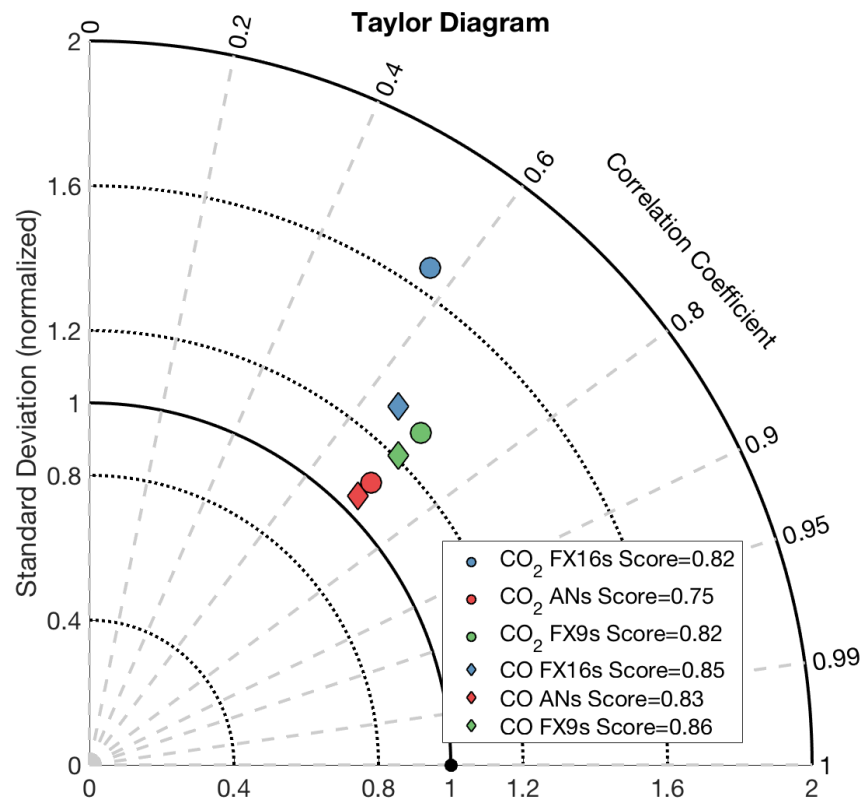
Figure S3. Taylor diagram for CAMS CO (diamonds) and CO_2 (circles) from FC9s (green), FC16s (blue), and ANs (red). Also shown are the Taylor scores.
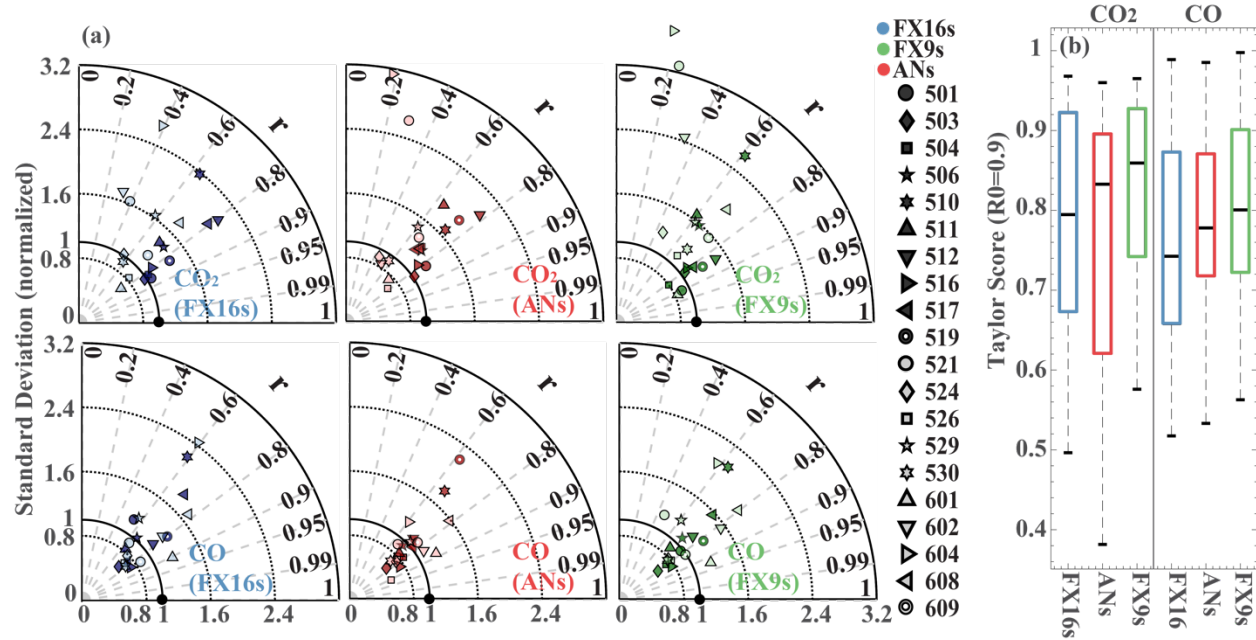
Figure S4. (a) Taylor diagrams for CAMS CO_2 (first row) and CO (second row) from 16-km forecasts (FC16s, left column), analyses (ANs, middle column), and 9-km forecasts (FC9s, right column) for individual flights (different symbols). (b) Boxplot of Taylor scores for CAMS CO_2 (left panel) and CO (right panel) from FC16s (blue), ANs (red), and FC9s (green).
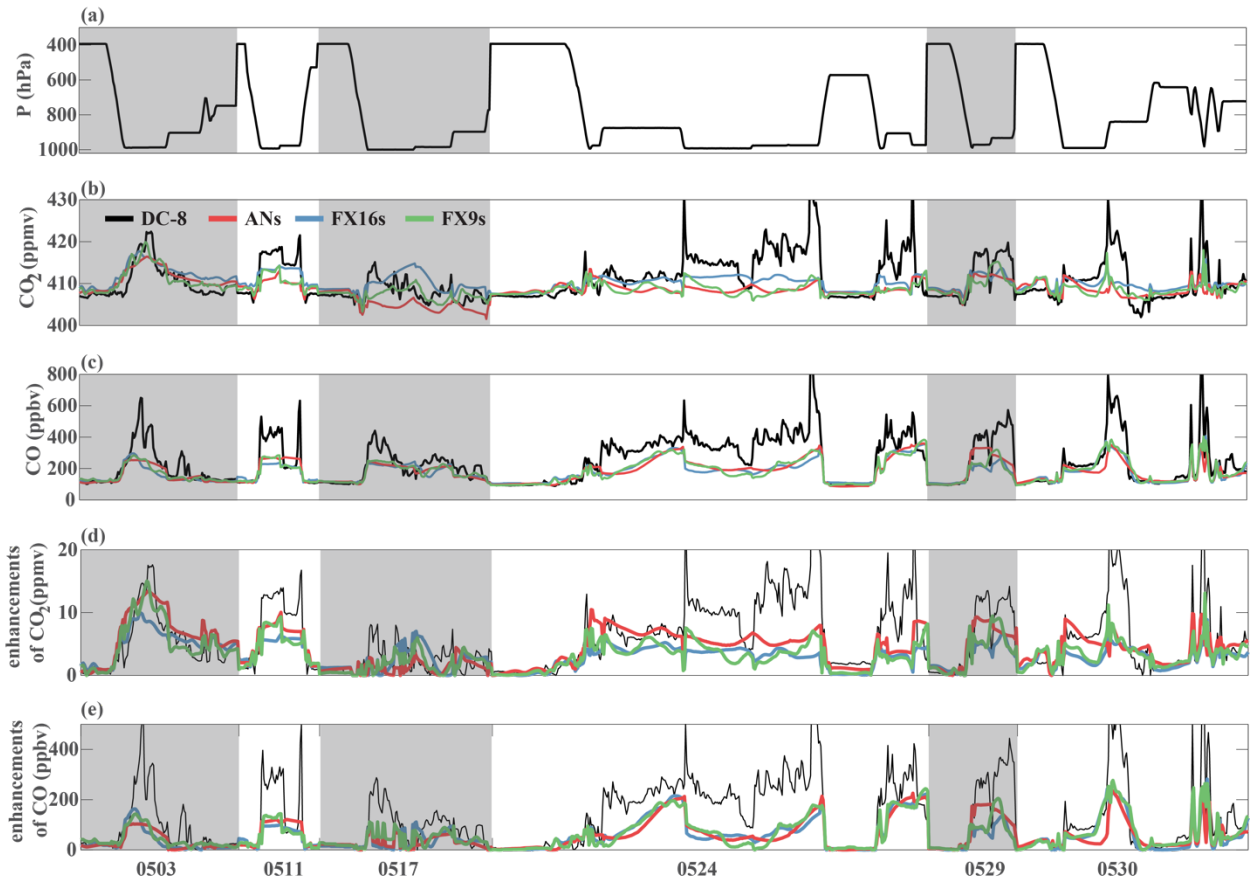
Figure S5. Time series of (a) pressure levels, (b) CO$_2$ concentrations and (d) their enhancements relative to background values, (c) CO concentrations and (e) their enhancements relative to background values along DC-8 aircraft tracks over the West Sea from measurements (black), 16-km forecasts (FC16s, blue), analyses (ANs, red), and 9-km forecasts (FC9s, green).
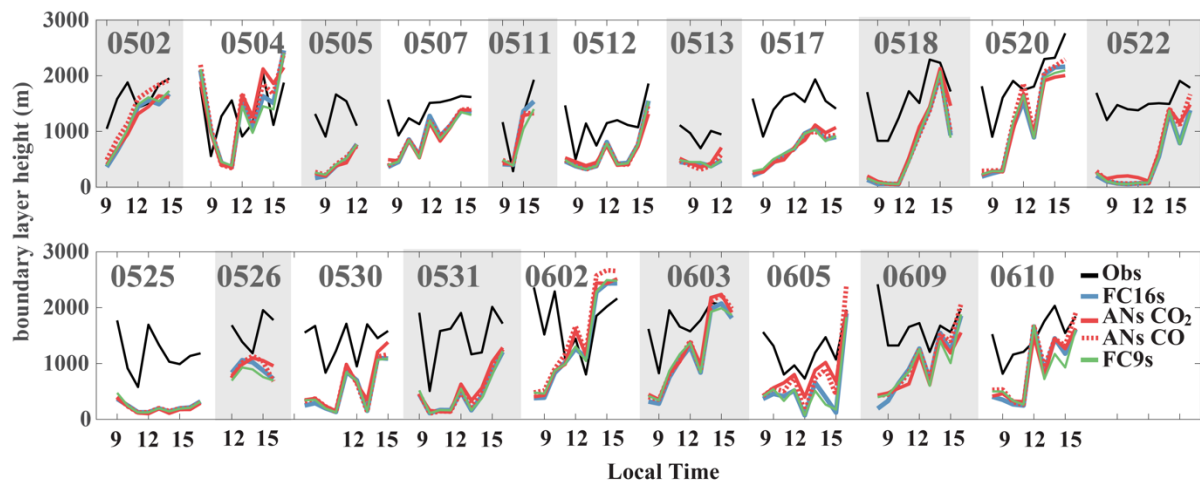
Figure S6. Hourly-average time series of the mixing layer heights derived from the airborne DIAL-HSRL measurements of aerosol backscatter (black) and corresponding boundary layer heights from the four CAMS configurations (colored) along the DC-8 flight track during KORUS-AQ.
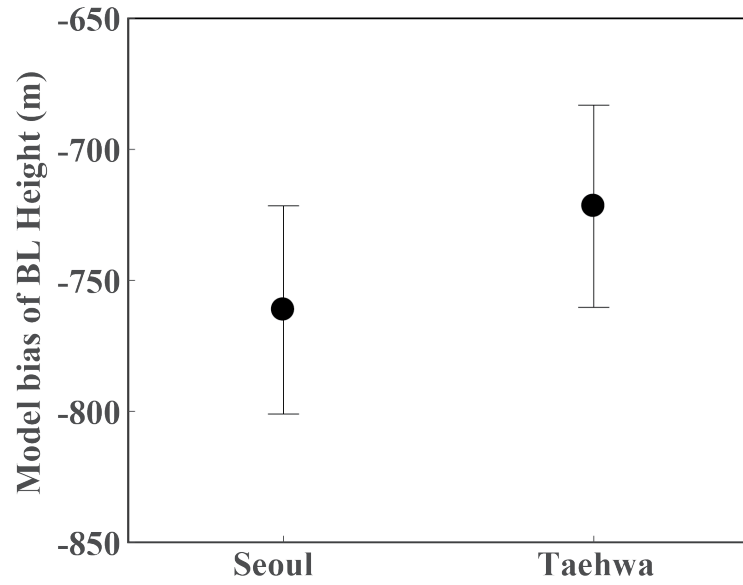
Figure S7. Model bias of boundary layer heights against boundary layer heights derived from the airborne DIAL-HSRL measurements of aerosol backscatter. Error bars represent standard deviations among the four CAMS configurations (i.e., FC16s, 80km ANs for CO, 40km ANS for CO_2, and FC9s).
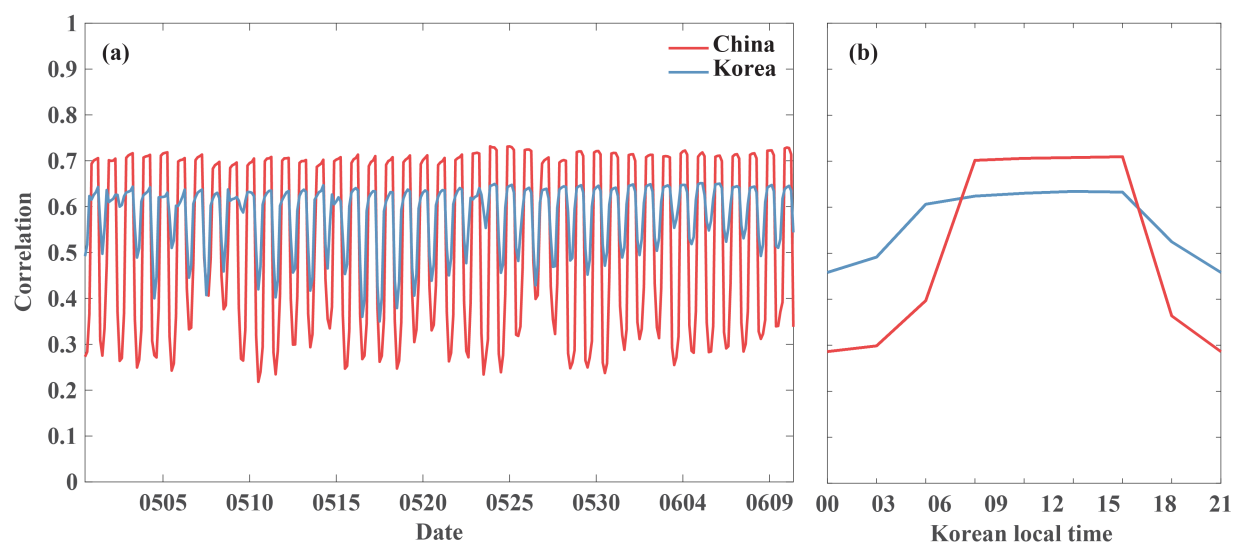
Figure S8. (a) Time series of spatial correlations between CO emissions and CO2 fluxes din CAMS over East China (which dominates Chinese contribution to the West Sea (Tang et al., 2018)) and Korea. (b) Averaged diurnal cycle of spatial correlations between CO emissions and CO2 fluxes in CAMS over East China and Korea.
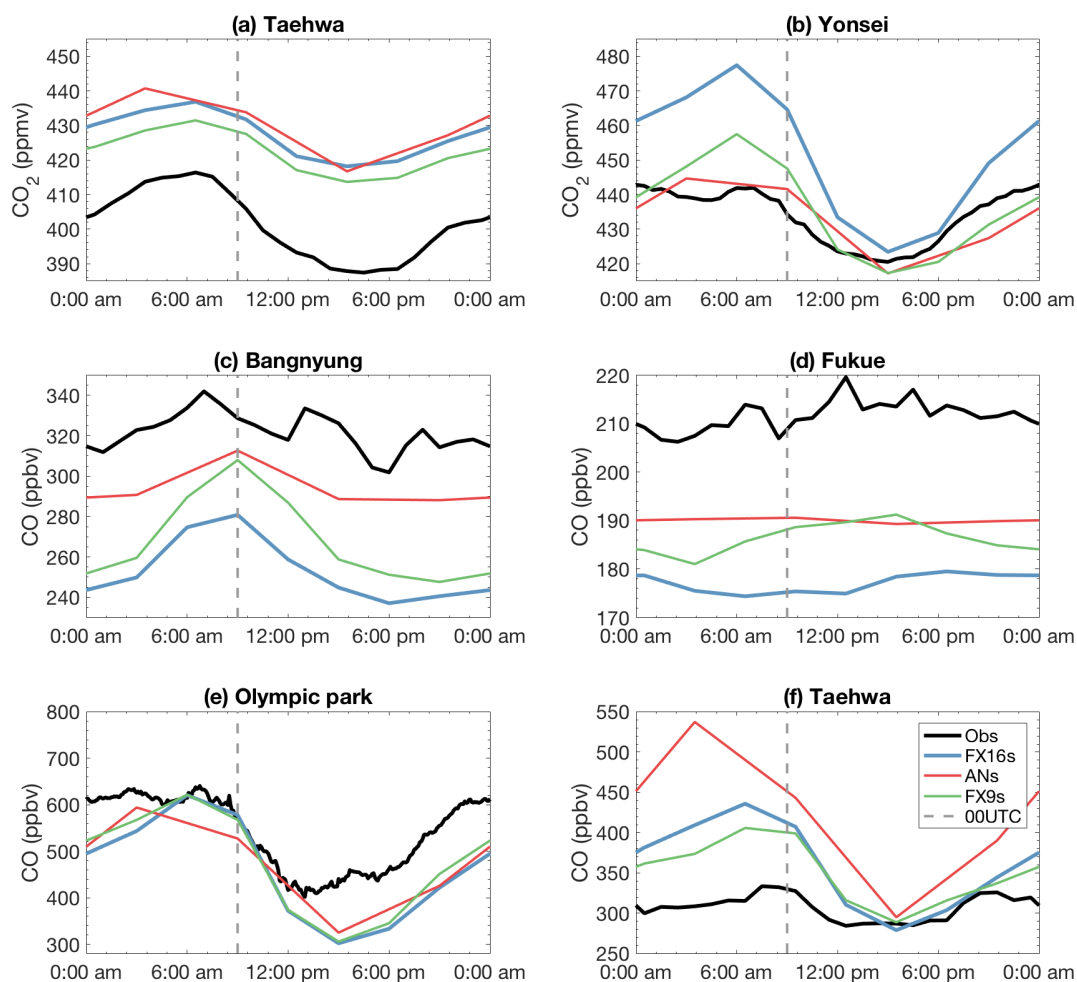
Figure S9. Diurnal cycles of CO_2 (a–b) and CO (c–f) concentrations averaged over days with available data during the KORUS-AQ period from observations (black), 16-km forecasts (FC16s, blue), analyses (ANs, red), and 9-km forecasts (FC9s, green) at fix ground sites, including (a, f) Taehwa, (b) Yonsei, (c) Bangnyung, (d) Fukue, and (e) Olympic park. CAMS values are averages across layers with pressure higher than 95% of the surface pressure.
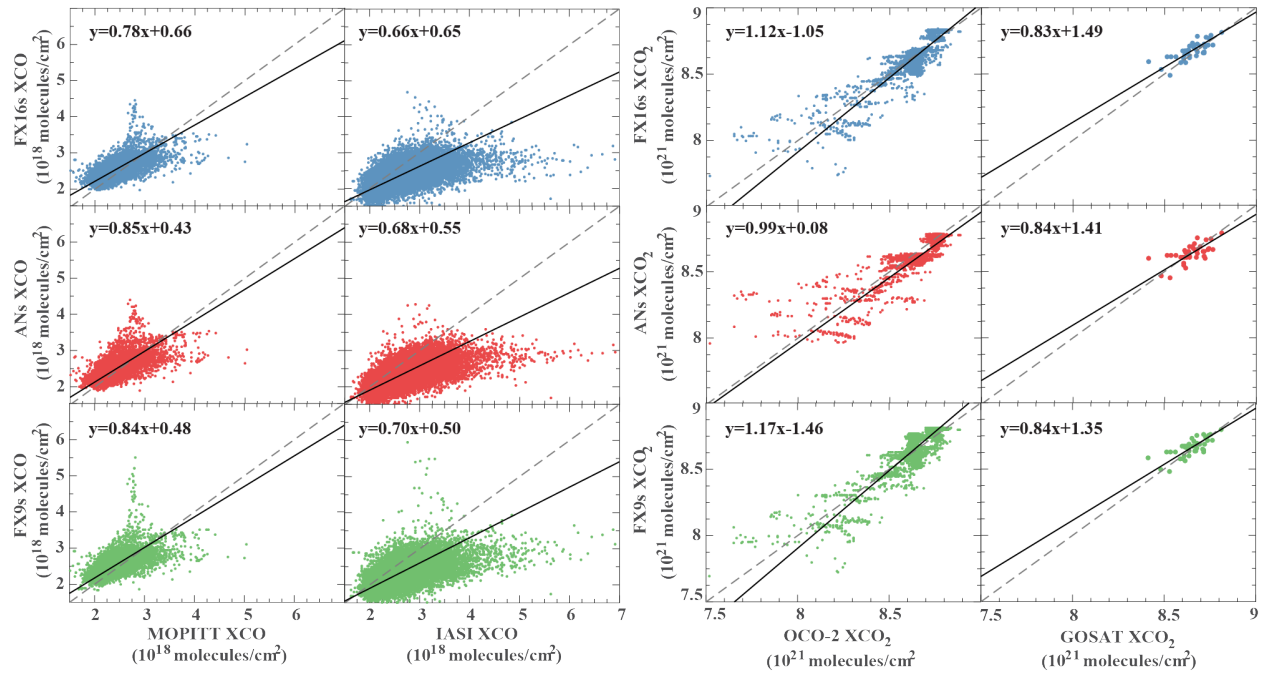
Figure S10. Comparisons between satellite observations and CAMS XCO and XCO2 from 16-km forecasts (FC16s, blue, 1st row), analyses (ANs, red, 2nd row), and 9-km forecasts (FC9s, green, 3rd row). The columns from left to right correspond to MOPITT XCO, IASI XCO, OCO-2 XCO2, and GOSAT XCO2, respectively.
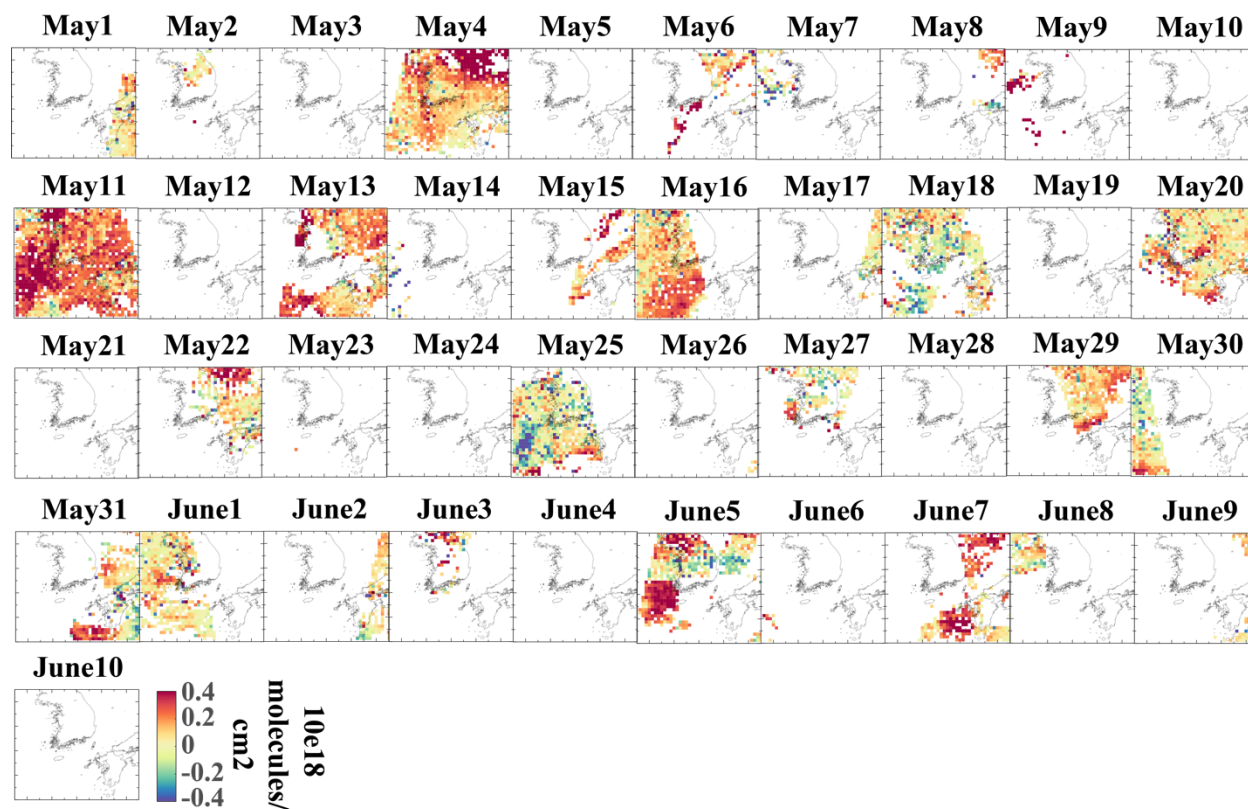
Figure S11. Daily spatial distributions of XCO biases in CAMS 9-km forecasts compared with MOPITT observations during the KORUS-AQ period (May 1 to June 10, 2016).